



# Influence of Gas Mixtures in GMAW of Modified 409M Ferritic Stainless Steel

*Up to 10% CO<sub>2</sub> with argon may be commercially utilized in the gas mixture for fabricating welded joints of 409M ferritic stainless steel*

BY M. MUKHERJEE, J. SAHA, P. KANJILAL, T. K. PAL, AND S. SISODIA

## ABSTRACT

The present study describes in detail the effect of shielding gas mixtures on the bead geometry, microstructure, and mechanical properties of gas metal arc welded modified ferritic stainless steel (409M) sheets (as received) of 4 mm thickness. The welded joints were prepared under spray (S) mode of metal transfer at same heat input using 308L austenitic filler metal and four different shielding gas mixtures, i.e., pure Ar, Ar + 5% CO<sub>2</sub>, Ar + 10% CO<sub>2</sub>, and Ar + 20% CO<sub>2</sub>. The welded joints were evaluated by means of microstructural changes, hardness, tensile strength, and toughness. The dependence of weld metal microstructure on shielding gas mixtures has been determined by bead geometry, Cr<sub>eq</sub>/Ni<sub>eq</sub> ratio, M<sub>s</sub>, M<sub>es</sub>, optical microscopy (OM), transmission electron microscopy (TEM), and electron probe microanalyzer (EPMA). It was observed that the variation in shielding gas mixture effectively manipulates the solid-state phase transformation and precipitation behavior of the welded joints. Variations in microstructure ultimately affect the mechanical properties of the weld metal as well as coarse-grained HAZ (CGHAZ). The present study concluded that up to 10% CO<sub>2</sub> may be commercially utilized in the shielding gas mixture for fabricating welded joints of 409M using 308L filler metal without deteriorating microstructural and mechanical properties.

## KEYWORDS

- Modified Ferritic Stainless Steel • Shielding Gas Mixtures • GMAW
- Microstructure • Mechanical Properties

## Introduction

The gas metal arc welding (GMAW) process is commonly used for fabricating various components of ferritic stainless steel. One of the unique characteristics of the GMAW process is the way molten metal is transferred across the arc. Metal transfer is controlled by several parameters, including current,

voltage, polarity, electrode extension, shielding gas composition, and electrode diameter. Previous work (Refs. 1, 2) reported that the microstructural constituents such as grain size, martensite content, and precipitation in ferritic stainless steel weldments are strongly dependent upon the variation in modes of metal transfer and heat input. The spray mode of metal transfer (S-mode) produces a greater

amount of grain boundary austenite along with lath martensite, which inhibits ferrite grain growth in the weld metal and induces higher strength and toughness (Ref. 1). However, the effect of martensite on mechanical properties is controversial and may promote hydrogen-induced cracking (Ref. 3).

The variation in shielding gas mixtures in the GMAW process has a direct impact on welding costs, and it also affects the weld quality through its influence on metal transfer. A mixture of carbon dioxide (CO<sub>2</sub>) and argon (Ar) is widely used as a shielding gas for arc welding processes (Ref. 4). Carbon dioxide is more plentiful, widely available, and two to three times less expensive than argon. Therefore, substantial savings are possible if welds are made with the addition of more CO<sub>2</sub> in an Ar-CO<sub>2</sub> mixture. However, weld bead quality and deposition rates often decrease with the increase of CO<sub>2</sub> in a binary Ar-CO<sub>2</sub> mixture (Ref. 5). Using uncoated steel electrodes and nonpulsed power supplies with direct current electrode positive (DCEP), Smith (Ref. 6) reported stable, axial type of free-flight transfer when the CO<sub>2</sub> concentrations in Ar-CO<sub>2</sub> mixture are less than 25%. Above 25% CO<sub>2</sub>, the operating characteristics of the process changed to repelled transfer during free-flight mode. However, quality welds can be made with 100% CO<sub>2</sub> at decreased deposition rates using short circuiting transfer. Also, the addition of CO<sub>2</sub> in the shielding gas increases the transition current

M. MUKHERJEE is a senior research fellow, J. SAHA is a graduate student, and T. K. PAL (tkpal.ju@gmail.com) is a professor, Metallurgical and Material Engineering Department, Jadavpur University, Kolkata, India. P. KANJILAL is a scientist SD (Mechanical), National Test House, Saltlake, Kolkata, India. S. SISODIA is general manager (Quality), Salem Steel Plant, Steel Authority of India Ltd., Salem, Tamil Nadu, India.

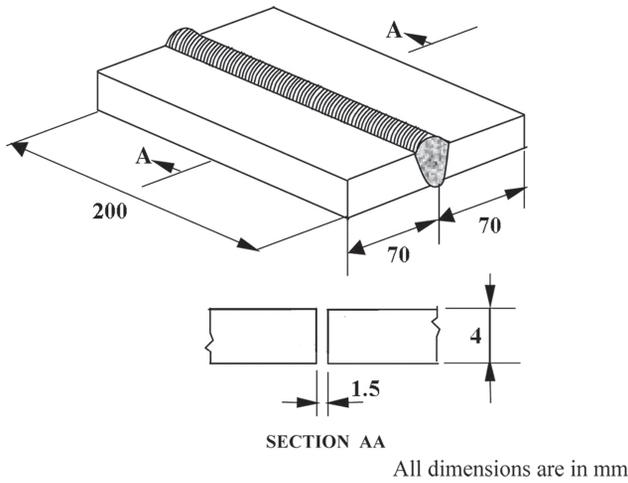


Fig. 1 — Weld preparation and test plate assembly.

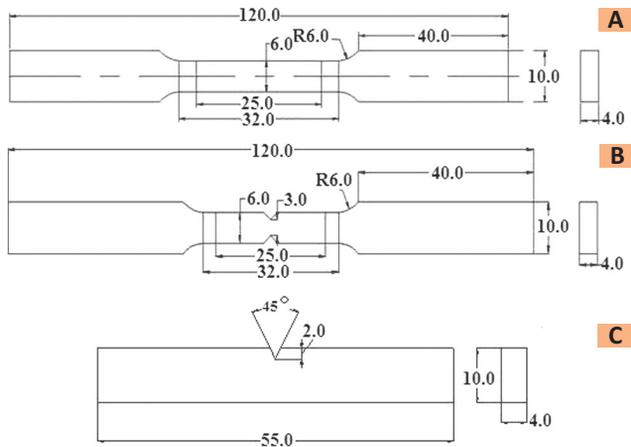


Fig. 3 — Dimensions. A — Unnotched tensile specimen; B — notched tensile specimen; C — subsize impact specimen.

and decreases the maximum droplet detachment frequency. The shielding gas not only affects the metal transfer but also determines the shape and penetration pattern. Several researchers have investigated the effect of CO<sub>2</sub> content on weld penetration with the variation in welding parameters and found that the weld penetra-

tion increases with the CO<sub>2</sub> content (Refs. 7, 8). The influence of shielding gas composition on the apparent weld shape as well as on the surface tension of the droplet travel between the electrode tip and weld pool were also studied (Refs. 9, 10). It appears that the shielding gas is one of the key factors that ultimately affects the microstructure and mechanical properties of the welds, mainly through the mode of metal transfer. However, available information concerning the effects of Ar and CO<sub>2</sub> shielding gas mixtures on the dissimilar weld joint of 409M ferritic stainless steel welded with 308L filler metal is very meager. Hence, it becomes imperative to study both from

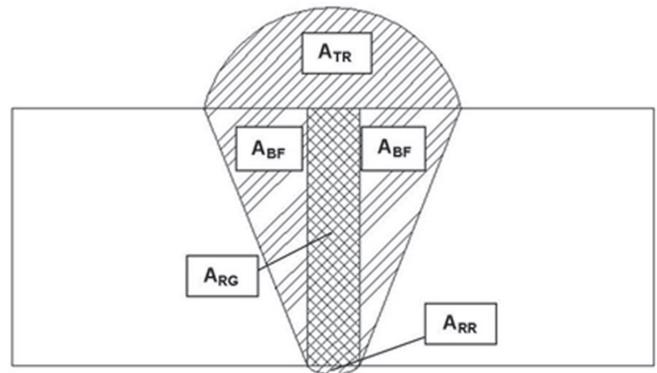


Fig. 2 — Schematic view of the different locations of the welded joint considered in graphical measurement of the area of weld deposit ( $A_{wd}$ ) and the area of base metal fusion ( $A_{BF}$ ).

an economical as well as technical point of view the effect of an increase in CO<sub>2</sub> content in a binary Ar-CO<sub>2</sub> mixture under spray mode, on the microstructural and mechanical properties of welded joints.

In the present study, ferritic-austenitic dissimilar welds (409M base plate and 308L filler metal) are made by varying the shielding gas mixture, namely pure Ar, Ar + 5%CO<sub>2</sub>, Ar + 10% CO<sub>2</sub>, and Ar + 20% CO<sub>2</sub>, under spray mode of metal transfer. The aim of the present work was to study the effect of various mixtures of Ar and CO<sub>2</sub> on the solid-state phase transformation, precipitation behavior, and mechanical properties of the GMA welded joints.

## Experimental Procedure

### Material

The hot-rolled sheets of 4-mm-thick 409M grade ferritic stainless steel were cut into required dimensions and used for the gas metal arc welding (GMAW) process. The details of weld joint preparation and test plate assembly are shown in Fig. 1. The chemical composi-

Table 1 — Chemical Compositions of Base Metal and Filler Metals

Type	Chemical Composition (in wt-%)										
SSP 409M											
Base metal	C%	Si%	Mn%	P%	S%	Cr%	Ni%	Mo%	Cu%	Nb%	N%
	0.030	0.463	0.79	0.029	0.014	11.10	0.31	0.033	0.026	0.017	0.01
308L Filler Metal	0.015	0.53	1.68	0.012	0.03	19.53	9.26	0.117	0.082	0.026	0.053

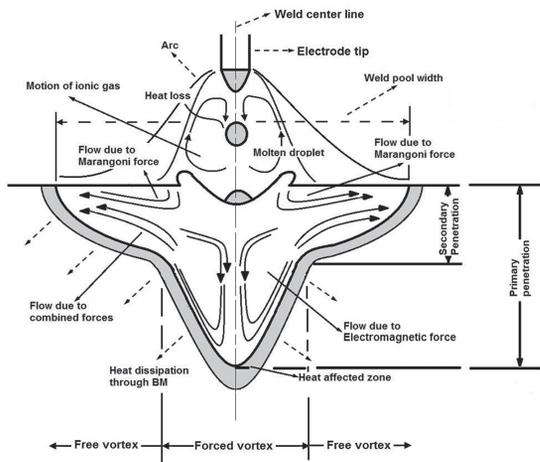


Fig. 4 — Schematic representation shows the effect of turbulent fluid flow induced in the weld pool by the combined result of different driving forces on the weld pool dimensions and shape.

tions of the base metal and austenitic 308L, 1.2-mm-diameter filler metal used are given in Table 1.

### Welding Procedure

The experiments were conducted using a water-cooled universal GMAW machine (Make: KEMPPPI, Finland; Model: EVOLUTION PRO 4200) using DC electrode positive (DCEP). The welding conditions and process parameters used to fabricate the joints are given in Table 2. The initial joint configuration was obtained by securing the plates in the flat position using tack welding. Square butt joints with a root opening of 1.5 mm were fabricated with the GMAW process using the selected welding parameters for the spray mode of metal transfer. To ascertain the operating mode, current and voltage waveforms were recorded by an oscilloscope during each welding run. The welding operations were performed using pure Ar, Ar + 5% CO<sub>2</sub>, Ar + 10%CO<sub>2</sub> and Ar + 20%CO<sub>2</sub> shielding

gas mixtures at constant heat input. All necessary care was taken to avoid joint distortion by applying proper clamping devices.

The soundness of all the welded plates was examined using radiography.

### Metallographic Study

The specimens for metallography study comprised of weld metal, heat-affected zone (HAZ), and base metal were polished using different grades of emery papers followed by a final polishing with a disc using diamond compound (2-µm particle size). The specimens were then etched with 10 mL hydrochloric acid, 0.5 g cupric chloride, and 10 mL ethanol for 10–15 s. Microstructural examination was carried out using a light optical microscope (Make: Carl ZEISS India Pvt. Ltd.; Model: Imager.A1m). The welded specimens were also examined under transmission electron microscope (TEM) (Make: Philips Ltd., Netherlands; Model: CM-70). The specimens from the weld metal and HAZ were prepared using a diamond cutting tool

and fine grades of emery papers up to 0.1 mm followed by a chemical etching/thinning process up to 10 µm.

### Dilution Calculation

The percentage dilution (D<sub>L</sub> %) of base metal was calculated from the geometrical characteristics of weld joints such as total area of weld deposit (A<sub>WD</sub>), area of top (A<sub>TR</sub>) and root (A<sub>RR</sub>) reinforcement, area of base metal fusion (A<sub>BF</sub>), and area of root opening (A<sub>RG</sub>), as schematically shown in Fig. 2. The estimation of A<sub>WD</sub>, A<sub>BF</sub>, and D<sub>L</sub> % was found out as follows (Refs. 1, 2):

$$A_{WD} = A_{RG} + A_{TR} + A_{BF} + A_{RR} \quad (1)$$

$$A_{BF} = A_{WD} - A_{RG} - A_{TR} - A_{RR} \quad (2)$$

$$D_L \% = \frac{A_{BF}}{A_{WD}} \times 100\% \quad (3)$$

### Calculation of Cr-Ni Equivalents and Martensite Transformation Temperatures

Weld metal compositions obtained

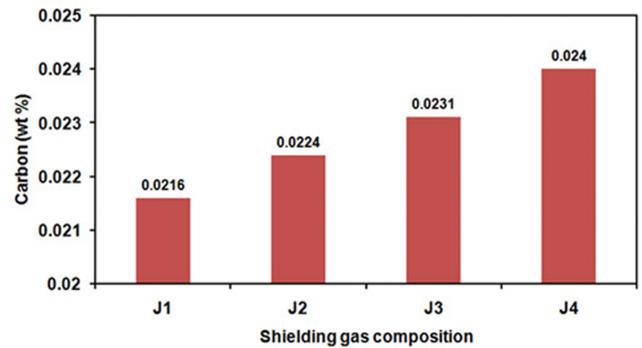
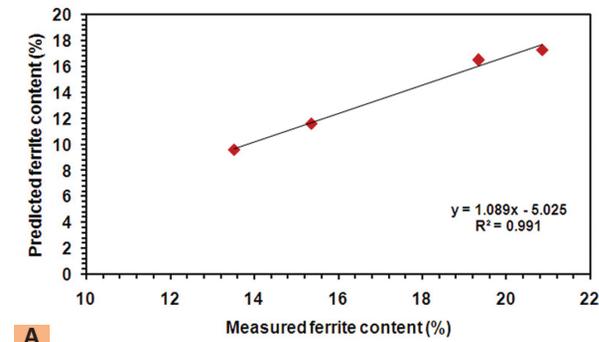


Fig. 5 — Optical emission spectroscopy reveals the variation of carbon content in different weld metals.

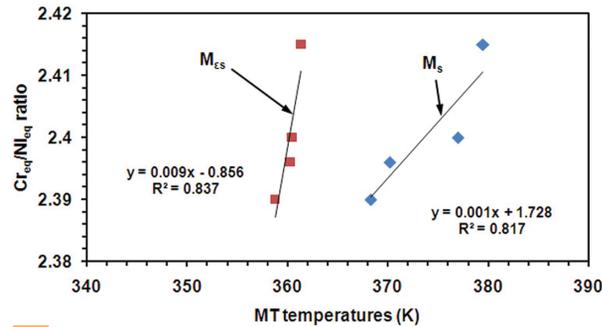
Table 2 — Welding Conditions and Process Parameters

Sample Specification	Current (A)	Voltage (V)	WFS (m/min)	WS (mm/min)	HI (kJ/mm)	Gas Mixture	GFR (L/min)
J1	240 ±10	28.0 ±0.7	7.0 ±0.1	500 ±5	0.72 ±0.5	100% Ar	15
J2						Ar + 5% CO <sub>2</sub>	
J3						Ar + 10% CO <sub>2</sub>	
J4						Ar + 20% CO <sub>2</sub>	

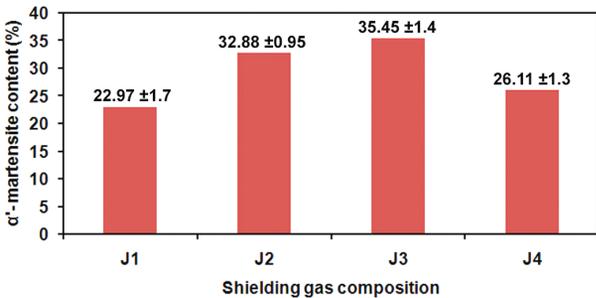
Note: WFS = wire feed speed; WS = welding speed; HI = heat input [(I × v × η × 60)/(WS × 1000)]; GFR = gas flow rate.



A



B



C

Fig. 6 — A — Predicted vs. measured ferrite content; B —  $Cr_{eq}/Ni_{eq}$  ratio vs. MT temperatures plot; C —  $\alpha'$ -martensite (mass %) of different weld metals.

from dilution were used to calculate the chromium equivalent ( $Cr_{eq}$ ) and nickel equivalent ( $Ni_{eq}$ ) values using the following equations (Ref. 11):

$$Cr_{eq} = Cr\% + Mo\% + 0.7 \times Nb\% \quad (4)$$

$$Ni_{eq} = Ni\% + 35 \times C\% + 20 \times N\% + 0.25 \times Cu\% \quad (5)$$

$$M_s (K) = A_3 - 199.8 \times (C + 1.4N) - 17.9 \times Ni - 21.7 \times Mn - 6.8 \times Cr - 45.0 \times Si - 55.9 \times Mo - 1.9 \times (C + 1.4N) \times (Mo + Cr + Mn) - 14.4 \times [(Ni + Mn) \times (Cr + Mo + Al + Si)]^{1/2} - 410 \quad (6)$$

$$M_{ES} (K) = A\epsilon - 710.5 \times (C + 1.4N) - 18.5 \times Ni - 12.4 \times Mn - 8.4 \times Cr + 13.4 \times Si - 1.6 \times Mo - 22.7 \times Al + 11.6 \times (C + 1.4N) \times (Mo + Cr + Mn) - 3.7 \times [(Ni + Mn) \times (Cr + Mo + Al + Si)]^{1/2} + 277 \quad (7)$$

where  $A_3$  is the  $\gamma \rightarrow \alpha$  phase transformation temperature of pure iron, and

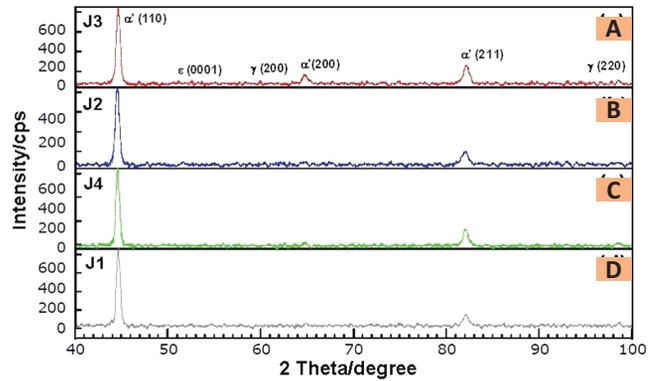


Fig. 7 — X-ray diffraction pattern collected from different welds. A — J3; B — J2; C — J4; D — J1.

In order to predict the presence of  $\alpha'$ - and  $\epsilon$ -martensite, martensite start temperature ( $M_s$ ) and  $\epsilon$ -martensite start temperature ( $M_{ES}$ ), i.e., martensite transformation temperatures, for different weld metals, were calculated using the following equations (Ref. 12):

$A\epsilon$  is the fictitious phase transformation temperature of  $\gamma \rightarrow \epsilon$ , about 390 K (Ref. 12).

### Grain Size Measurement

The grain sizes of the welds were evaluated by the linear intercept method from the optical micrographs using image analyzing software (Axio-Vision/AxioCam version 4.6). An average of five readings was reported.

### Ferrite and Martensite Measurement

The ferrite percent of each weld metal was evaluated using Feritscope® FMP30, and an average of ten readings was reported. The actual  $\alpha'$  martensite content ( $C_{\alpha'}$ ) had been computed from Feritscope data F (% ferrite) using relation  $C_{\alpha'} (\text{mass } \%) = 1.7 \times F$  (Ref. 13), and an average of five readings was reported.

### Microhardness Testing

A microhardness survey was made on flat metallographic specimens across the joints in a Vickers' microhardness testing machine (Make: LECO Co., USA; Model: LM248AT) using 100 gf load at an interval of 500  $\mu\text{m}$ .

### Tensile Testing

Two different tensile specimens were prepared as shown in Fig. 3A and B. The unnotched smooth transverse tensile specimens were prepared to evaluate transverse tensile properties.

Table 3 — Average Bead Geometry for Different Welds

Sample Specification	Bead Height (H) (mm)	Bead Width (W) (mm)	Height to Width Ratio	Toe Angle (Degree)
J1	2.2 ± 0.46	9.82 ± 0.65	0.224 ± 0.03	43.4 ± 2.0
J2	2.15 ± 0.4	9.89 ± 0.50	0.217 ± 0.03	42.6 ± 2.3
J3	2.03 ± 0.38	10.12 ± 0.44	0.201 ± 0.03	41.3 ± 2.0
J4	1.88 ± 0.40	10.44 ± 0.7	0.180 ± 0.03	40.7 ± 2.2

The notched specimens were prepared by placing the V-notch on weld metal and base metal to evaluate notched tensile properties. All the tensile tests were conducted in 100 kN, electro-mechanical controlled universal testing machine (Make: INSTRON LIMITED, England; Model: INSTRON-8862) as per ASTM E8M-04 guidelines. An average of three readings was reported.

### Charpy Impact Testing

Subsize Charpy impact specimens, due to smaller plate thickness, were prepared as shown in Fig. 3C to evaluate the impact toughness of the weld metal. Impact testing was performed at room temperature using a pendulum-type impact testing machine as per ASTM E23-07 and an average of four readings was reported.

### Scanning Electron Microscopy

The fractured surfaces of impact tested specimens were examined under scanning electron microscope (SEM) (Make: JEOL Ltd., Japan; Model: LSM-6360) to understand the micromechanism in fracture.

## Results and Discussion

### Effect of CO<sub>2</sub> Content on Variation of Weld Profile

Shielding gas compositions offer different physical and chemical properties, such as thermal conductivity, ionization energy, and chemical activity, which affect the arc behavior, and consequently the weld bead profiles as presented in Table 3. It can be observed from Table 3 that the bead height and toe angle decrease and bead width increases with an increase in CO<sub>2</sub> content. The reinforcement height, width, and toe angle are significantly influenced by the Marangoni force (Refs. 14, 15) due to more negative surface tension temperature gradient ( $\delta\gamma/\delta T$ ) with an increase in oxygen potential (OP) of the shielding gas mixtures (Ref. 9). Oxygen potential of the shielding gas mixtures can be derived using the equation  $OP = O_2 + \mu CO_2$ , where  $\mu$  is the oxidizing factor and taken as 0.7 as per existing litera-

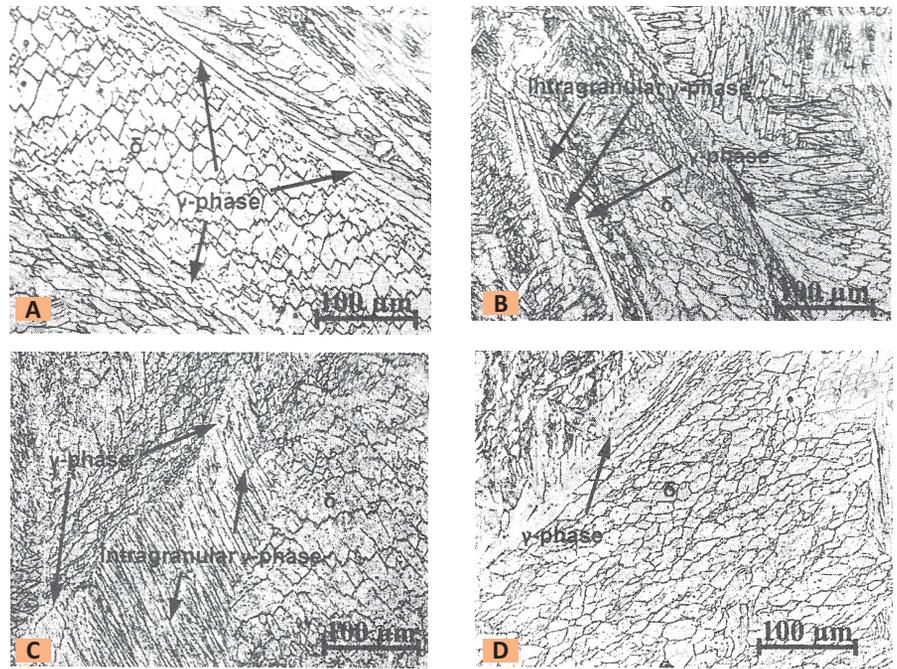


Fig. 8 — Optical micrograph of welds. A — J1; B — J2; C — J3; D — J4 shows different morphologies of  $\gamma$  phase.

Table 4 — Dilution Calculations for Different Welds

Sample Specification	$A_{BF}$ (mm <sup>2</sup> )	$A_{WD}$ (mm <sup>2</sup> )	$D_L$ (%)
J1	22.43 ± 5.0	48.5 ± 8.0	46.24 ± 3.0
J2	16.65 ± 6.4	35.46 ± 9.0	46.95 ± 4.8
J3	17.33 ± 6.6	36.62 ± 8.4	47.32 ± 5.8
J4	21.27 ± 7.4	44.81 ± 8.2	47.46 ± 6.6

ture (Ref. 16).

Therefore, an increase in CO<sub>2</sub> content increases the OP and governs the formation of extremely volatile oxide films, which have lower surface tension compared to the base metal (Refs. 9, 17). Hence, more negative  $\delta\gamma/\delta T$  pushes the molten fluid in the outward direction (away from the weld pool center) as schematically shown in Fig. 4A, which ultimately leads to lower bead height and wider bead width. This is also the possible reason why lower toe angles are obtained with higher CO<sub>2</sub> content.

Again, the arc force was found to be related to the arc length and defined by the following equation (Ref. 26):

$$F_{arc} = 3.57 \times 10^{-5} \times \frac{I^2}{l_{arc}^{1/2}} \quad (8)$$

where  $F_{arc}$  is the arc force,  $I$  is the mean current, and  $l_{arc}$  is the arc length. It is

generally accepted that the thinner isothermal distribution, lower thermal conductivity with less heat flow associated with the pure Ar due to higher ionization potential when compared to binary mixtures, leads to a higher arc length and consequently to a lower arc force (Refs. 9, 17). On the contrary, due to higher heat flow associated with gas mixtures containing higher CO<sub>2</sub>, the radial distribution of the arc temperature is more uniform and its length should be shorter for the same heat intensity (Ref. 17). Hence, mixtures with higher amounts of CO<sub>2</sub> will lead to higher arc force and consequently deeper lateral penetration.

### Prediction of Weld Metal Microstructure

The  $D_L$  % is calculated from the geometrical characteristics of the welded joint as schematically shown in Fig. 2. The estimation of  $A_{WD}$ ,  $A_{BF}$ , and  $D_L$  % are

**Table 5 — Composition of Different Weld Metals (wt-%) Derived from Dilution and  $Cr_{eq}$ ,  $Ni_{eq}$ ,  $Cr_{eq}/Ni_{eq}$  Ratio and Martensite Transformation Temperatures ( $M_s$  and  $M_{es}$ )**

Sample Specification	J1	J2	J3	J4
C	0.0219 ±0.0004	0.022 ±0.0007	0.022 ±0.0009	0.022 ±0.001
Si	0.499 ±0.002	0.499 ±0.003	0.498 ±0.004	0.498 ±0.004
Mn	1.268 ±0.02	1.262 ±0.04	1.259 ±0.05	1.257 ±0.06
P	0.020 ±0.0005	0.020 ±0.0008	0.020 ±0.0009	0.020 ±0.001
S	0.023 ±0.0005	0.022 ±0.0007	0.022 ±0.0009	0.022 ±0.001
Cr	15.63 ±0.25	15.57 ±0.4	15.540 ±0.48	15.530 ±0.55
Ni	5.122 ±0.26	5.058 ±0.43	5.025 ±0.52	5.012 ±0.6
Mo	0.078 ±0.003	0.078 ±0.004	0.077 ±0.005	0.077 ±0.005
Cu	0.056 ±0.002	0.056 ±0.002	0.056 ±0.003	0.0554 ±0.004
Nb	0.022 ±0.0003	0.022 ±0.0004	0.0215 ±0.0005	0.0217 ±0.0005
N	0.0331 ±0.0013	0.0328 ±0.002	0.0326 ±0.002	0.0325 ±0.003
$Cr_{eq}$	15.72 ±0.25	15.69 ±0.23	15.63 ±0.32	15.60 ±0.45
$Ni_{eq}$	6.655 ±0.36	6.52 ±0.1	6.47 ±0.27	6.58 ±0.62
$Cr_{eq}/Ni_{eq}$	2.36 ±0.1	2.40 ±0.15	2.415 ±0.17	2.37 ±0.12
$M_s$ [K(°C)]	368.3 (95.3) ±19.1	377.04 (104.04) ±20.7	379.5 (106.5) ±23.9	370.2 (97.2) ±17.4
$M_{es}$ [K(°C)]	358.8 (85.8) ±8.91	360.5 (87.5) ±15.1	361.4 (88.4) ±18.23	360.3 (87.3) ±11.8

found out from Equations 1, 2, and 3, respectively. The effect of shielding gas compositions on the geometrical characteristics of the weld with respect to  $A_{WD}$ ,  $A_{BF}$ , and  $D_L$  is given in Table 4. As expected, weld metal prepared with pure Ar shielding (J1) leads to lower dilution. Other weld metals have comparatively higher  $D_L$  and it increases with the increase in  $CO_2$  content. Weld metal compositions obtained from dilution calculation are shown in Table 5. Furthermore, optical emission spectroscopy (as per ASTM 1086-94) of the weld metal was carried out to ascertain the compositions obtained from dilution. Only the spectroscopic result of carbon content, as shown in Fig. 5, differs from the dilution calculation, due to the fact that in dilution calculation the absorption of carbon from dissociated shielding gas mixtures (during welding) was not considered.

The final weld metal compositions were then used to calculate the chromium equivalent ( $Cr_{eq}$ ) and nickel equivalent ( $Ni_{eq}$ ) values using Equations 4 and 5 along with  $Cr_{eq}/Ni_{eq}$  ratios, and the values are also given in Table 5. The variation in  $Cr_{eq}$  and  $Ni_{eq}$  among four different welds (J1, J2, J3, and J4) is due to significant variation in wt-% of Cr and Ni (Table 5). The  $Cr_{eq}$  and  $Ni_{eq}$  values were then incorporated in the modified WRC-1992 diagram (Ref. 18) to predict the ferrite number of the welds. The predicted ferrite ( $\delta$ ) content of the entire weld varied with shielding gas composition used. It is interesting to note that the

predicted ferrite ( $\delta$ ) content and the measured ferrite ( $\delta$ ) content for different weld metals are very close to each other as shown in Fig. 6A. Present investigation reveals that welds J2 and J3 contain comparatively a higher amount of ferrite ( $\delta$ ) than welds J1 and J4. This may be due to the higher  $Cr_{eq}/Ni_{eq}$  ratio of J2 and J3 welds compared to J1 and J4 as shown in Table 5. Higher  $Cr_{eq}/Ni_{eq}$  ratio increases the stability of the  $\delta$ -ferrite by shifting the solidification line away from the triple point (i.e., L +  $\gamma$  +  $\delta$  zone) into the  $\delta$ -ferrite region.

In order to understand the phase transformation in different welds, the presence of  $\alpha'$ - and  $\epsilon$ -martensite,  $\alpha'$ -martensite start temperature ( $M_s$ ), and  $\epsilon$ -martensite start temperature ( $M_{es}$ ), i.e., martensite transformation temperatures, were calculated using Equations 6 and 7, respectively, and the values are given in Table 5. The welds in general have lower  $M_{es}$  temperature values compared to  $M_s$  temperature (Table 5), and therefore,  $\gamma \rightarrow \alpha'$  transformation will take a predominant role over  $\gamma \rightarrow \epsilon$  transformation (Ref. 12). However,  $M_s$  and  $M_{es}$  values for J1 and J4 being very close (less than 10°C) to each other compared to welds J2 and J3, the possibility of the  $\epsilon$ -martensite present in J1 and J4 welds will be greater. Nevertheless, it is well known that  $\gamma \rightarrow \alpha'$  transformation has more thermodynamical stability over  $\gamma \rightarrow \epsilon$  transformation (Ref. 19) and thus under any stress such as residual stress during welding,  $\epsilon$ -martensite will

transform into  $\alpha'$ -martensite (Ref. 20). Therefore, it can be assumed that the weld metals should contain  $\alpha'$ -martensite along with some  $\epsilon$ -martensite in their final microstructure. Also, martensite transformation temperatures have been correlated with  $Cr_{eq}/Ni_{eq}$  ratios of different welds as shown in Fig. 6B. The weld metal compositions in terms of  $Cr_{eq}/Ni_{eq}$  ratio have created a variation in the martensite transformation temperatures among the welds, and hence, the amount of martensite laths. Accordingly, J2 and J3 having higher  $Cr_{eq}/Ni_{eq}$  ratio and martensite transformation temperatures than welds J1 and J4 (Table 5) should provide higher amount of martensite laths. To validate the possibility of a higher amount of martensite formation in welds J2 and J3,  $\alpha'$ -martensite content in mass % has been determined and the values are presented in Fig. 6C. It indicates that J2 and J3 have higher amounts of  $\alpha'$ -martensite than welds J1 and J4. This observation can also be supported by the X-ray diffraction patterns of welds as shown in Fig. 7, which depicts major peak intensities of bcc phase ( $\alpha'$ ), whereas austenite (fcc) phase does not differ significantly, indicating primary ferrite solidification. Therefore, it is exciting to note that, under the same heat input or cooling rate (Table 2), the amount of solid-state phase transformation is solely dependant upon the chemical composition of the weld metal, which is the result of variation in shielding gas compositions.

## Evolution of Weld Metal Microstructure

The optical micrograph in Fig. 8 shows that all the weld metal primarily consists of three phases, i.e., ferrite ( $\delta$ ), austenite ( $\gamma$ ), and martensite ( $\alpha'$ ). However, there are some noticeable variations among the micrographs of different welds. In Fig. 8A and D, austenite is revealed as a thin layer of grain boundary austenite or Widmanstätten austenite. On the other hand, Fig. 8B and C show more complex microstructures for welds J2 and J3. The area represented by the micrographs (Fig. 8B and C) has undergone a growth of grain boundary austenite in the interfaces between  $\delta$ -ferrite grains and a small portion of intragranular austenite within the  $\delta$ -ferrite grains. From the micrographs, it is clear that all the microstructures have primary ferrite and grain boundary austenite at room temperature.

The coarse areas of  $\alpha'$ -martensite and the fine laths of  $\epsilon$ -martensite (Ref. 1) in the welds are clearly illuminated in TEM micrographs under the bright field as shown in Fig. 9A–D. In welds J1 and J4 (Fig. 9A and D), formation of  $\alpha'$ -martensite is initiated from  $\epsilon$ -martensitic plates during cooling, which is considered as an intermediate phase in solid-state phase transformation ( $\gamma \rightarrow \epsilon \rightarrow \alpha'$ ) (Refs. 2–4), whereas, Fig. 9B and C reveal that in welds J2 and J3 martensite laths nucleated from dislocation pile-ups and the observed growth suggests that it is influenced by these dislocations (Ref. 21). A close look into TEM micrographs of different welds also shows that J2 and J3 have contributed a greater amount of martensite than welds J1 and J4.

Depending on the  $Cr_{eq}/Ni_{eq}$  ratio (Table 5), in the present study, the solidification mode of all weld metals can be categorized in the following way (Refs. 22, 23):

F mode:  $L \rightarrow L + \delta \rightarrow \delta + \gamma$ :

$Cr_{eq}/Ni_{eq} > 1.95$

F mode of solidification results in complete formation of ferrite, which may partially transform into austenite during cooling and ultimately leads to the formation of Widmanstätten structure (Ref. 22). However, depend-

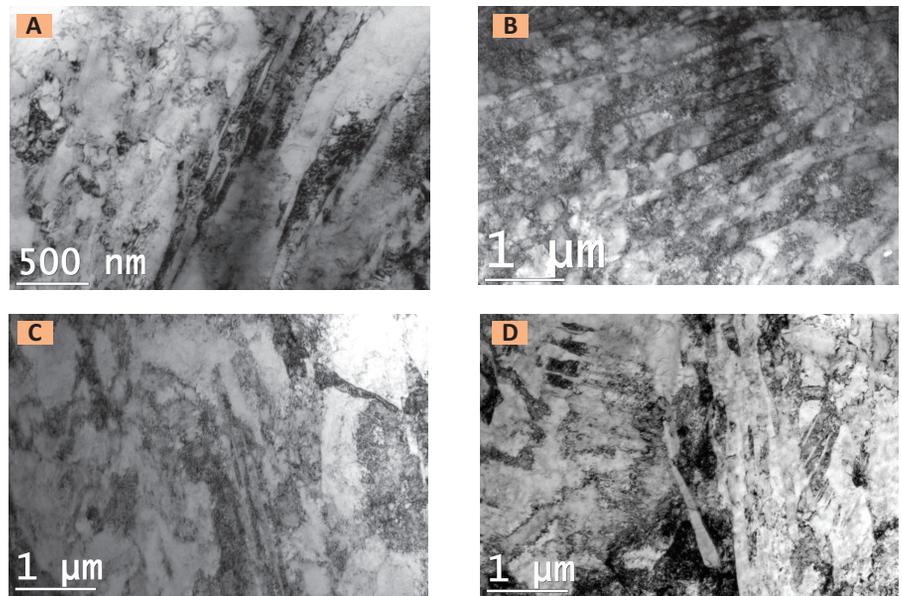


Fig. 9 — Bright field TEM micrograph of welds. A — J1; B — J2; C — J3; D — J4, shows the presence of austenite ( $\gamma$ ) along with  $\alpha'$ -martensite and  $\epsilon$ -martensite.

Table 6 — Average Hardness Values of weld and HAZ

Sample Specification	Avg. Hardness of Weld	Avg. Hardness of HAZ
J1	341.2 $\pm$ 16.7	309.4 $\pm$ 12.4
J2	361.4 $\pm$ 14.65	317.6 $\pm$ 18.8
J3	367.2 $\pm$ 15.83	320.9 $\pm$ 19.4
J4	356.7 $\pm$ 9.2	322.1 $\pm$ 22.7

ing upon the metastability of the phases, due to variation in weld composition, solidification, and transformation, can occur in different ways, i.e., the precipitation of primary ferrite, plus three-phase reaction (ferrite, austenite, and liquid) at the terminal solidification stage, and  $\delta \rightarrow \gamma$  continuing below the solidus line (Ref. 23). Hence, the final microstructure should consist of vermicular  $\delta$  as a primary phase within the dendrite arms enveloped by the  $\gamma$ -phase (Ref. 22). Lower  $Cr_{eq}/Ni_{eq}$  ratios of J1 and J4 (Table 5) can shift the weld composition toward the three-phase reaction zone ( $L + \delta + \gamma$ ) during solidification and increase the stability of  $\gamma$ -phase. It is worthwhile to mention here that J2 and J3 welds having higher  $Cr_{eq}/Ni_{eq}$  ratios and martensite transformation temperatures create more metastable  $\gamma$ -phase and should produce a greater amount of lath martensite (Fig. 6C) during solid-state phase transformation ( $\gamma \rightarrow \alpha'$ ) (denoted as  $\alpha'$ ) (Ref. 1).

From the observation, it can be elu-

cidated that after complete solidification and transformation, the weld microstructure should contain primary ferrite, austenite, and lath martensite at room temperature. Consequently, primary solidification processes exclusively depend upon the composition of weld metal in terms of  $Cr_{eq}/Ni_{eq}$  ratios.

The grain size of the weld metal was evaluated from the optical micrographs and the values are shown in Fig. 10. According to Fig. 10, the weld metal has finer grains compared to the coarse-grained HAZ (CGHAZ), and became more or less comparable with the base metal irrespective of shielding gas mixture used. It is interesting to note that 10%  $CO_2$  (J3) produces the finest grain structure among the welds. However, the grain size of weld J2 is very close to that of J3. Hence, welds J2 and J3 produce comparatively fine grain microstructure compared to J1 and J4. As discussed previously, metastability in weld structure enhances  $\delta \rightarrow \gamma$  transformation during cooling and perhaps controls the grain growth in weld metals J2

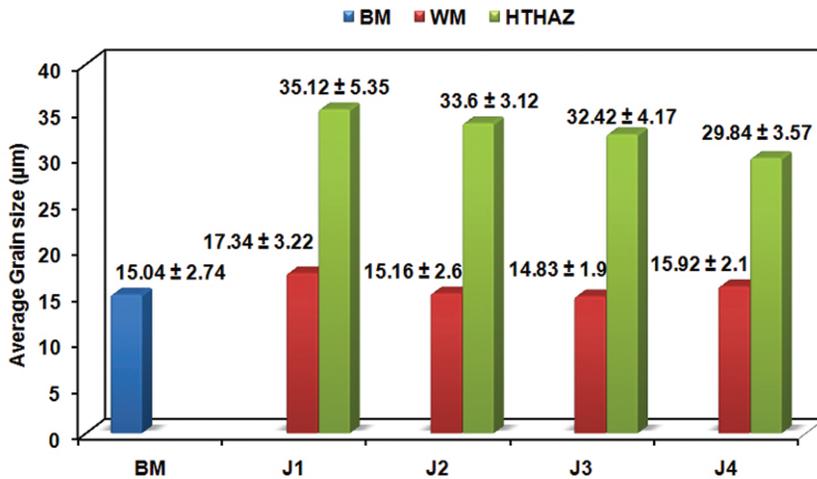


Fig. 10 — Average grain size of the weld metal and HTHAZ.

Table 7 — Tensile Test Results of Unnotched Base Metal and Welded Joints

Sample Specification	YS (MPa)	UTS (MPa)	Elongation	Location of Fracture
BM	312.2 ±17.4	483.1 ±21.1	29.8 ±1.37	BM
J1	314.3 ±8.2	466.8 ±13.7	24.1 ±0.98	BM
J2	308.1 ±9.3	473.8 ±10.4	22.7 ±1.24	BM
J3	320.2 ±5.7	471.2 ±7.6	23.1 ±0.99	BM
J4	328.5 ±8.8	477.3 ±11.7	22.4 ±1.13	BM

and J3 due to formation of more metastable  $\gamma$  phase along the grain boundary. Conversely, the other two welds (J1 and J4) have a relatively stable structure with less transformation, which is somewhat unable to restrict grain growth.

Furthermore, EPMA results, as shown in Fig. 11, reveal the segregation and/or concentration pattern of major alloying elements present in different weld metals. Among these, concentration of carbon is most important because it governs the nature of carbide precipitation in weld metal due to the absorption of carbon through the gas metal reaction. In unstabilized FSS alloys, these precipitates are primarily chromium-rich carbides ( $M_{23}C_6$ ) (Ref. 24). The carbide precipitation in welds J1, J2, and J3 is discontinuous and mainly occurs along the grain boundary (Fig. 11A-C), whereas, in weld metal J4, both inter- and intragranular type of discontinuous precipitation has been recognized (Fig. 11D). Figure 11B-D reveals the amount of carbide precipitation in the welds increases with the increase in  $CO_2$  content from 5% to 20%  $CO_2$  in

shielding gas mixture.

Earlier work reported that these precipitates form due to the supersaturation of carbon in the ferrite phase at elevated temperatures (Ref. 25). The ferrite-ferrite ( $\delta/\delta$ ) grain boundaries are most preferable site for Cr segregation and carbide formation as shown schematically in Fig. 12 due to the negligible presence of austenite (Ref. 26). Therefore, all the welds have grain boundary carbide precipitates mainly along the  $\delta/\delta$  grain boundary regions. However, the formation of  $\gamma$ -phase and  $\alpha'$  martensite along the grain boundary (Fig. 9) should reduce the tendency to form carbide precipitation (Ref. 27). These phases can significantly alter the alloy segregation by absorbing free carbon rejected from ferrite during solidification and reduce the Cr segregation along the grain boundary (Ref. 27). Hence, existence of such phases (i.e.,  $\gamma$  phase and  $\alpha'$  martensite) along the grain boundary is the potential cause of irregular or discontinuous carbide precipitation (Fig. 11B-D). Figure 12A-C schematically illustrates the precipitation behavior observed in different welds.

Pure Ar (J1) produces lesser and smaller amounts of precipitates (Fig. 12A) due to the fact that the base metal and the filler metal have low carbon content and there are no other sources of carbon addition through diffusion, absorption, and migration due to inert arc environment.

Increasing  $CO_2$  content (welds J2 and J3) in the arc atmosphere increases the gas metal reaction (between high-temperature ionic gas and molten pool) and absorbs more carbon into the weld pool (Fig. 5) due to dissociation of  $CO_2$  at a high temperature. These absorbed or migrated carbons can easily react with the potent carbide formers (i.e., Cr, Fe, etc.) and produces higher amount of precipitates along the grain boundary — Fig. 12 B. However, when the  $CO_2$  content is high enough (i.e., 20%  $CO_2$  in weld metal J4) in the arc atmosphere some migrated carbon may able to react with the potent carbide formers situated in the intragranular spaces and develop intragranular precipitates — Fig. 12C.

Therefore, from the above observations, it can be postulated that three types of microstructural combinations are possible in the fusion zone as schematically shown in Fig. 13. First, stable austenite has been formed together with a lower amount of martensite formation and less carbide precipitation along the grain boundary — Fig. 13A. Weld J1 with pure Ar shielding typically has this type of microstructure. Second, metastable austenite has been formed together with higher amount of martensite formation and moderate discontinuous carbide precipitation — Fig. 13b. Welds J2 and J3 with 5% and 10%  $CO_2$ , respectively, show this type of microstructure. Third, stable austenite was formed together with a low martensite formation and higher precipitates — Fig. 13C. Weld metal J4 with 20%  $CO_2$  shielding typically has this type of microstructure.

### Evolution of CGHAZ Microstructure

The typical coarse-grained HAZ (CGHAZ) microstructure of different welded joints as shown in Fig. 14 reveals ferrite with some martensite. The CGHAZ adjacent to the weld in-

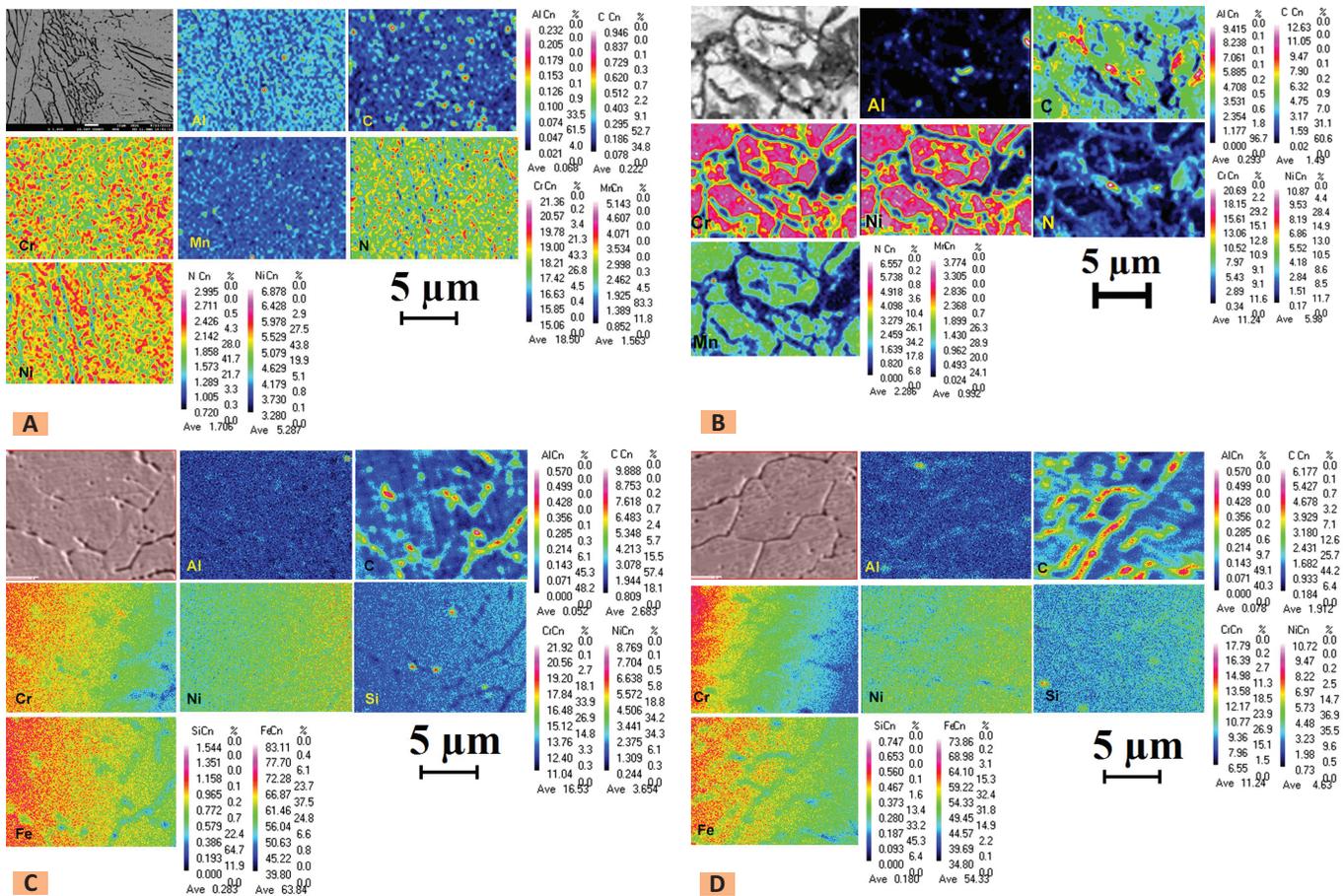


Fig. 11 — EPMA results of welds, A — J1; B — J2; C — J3; D — J4, show distribution of major alloying elements.

terface represents base metal heated above the  $A_3$  temperature (i.e.,  $910^\circ\text{C}$ ) during the weld thermal cycle, and is characterized by  $\delta$ -ferrite grains surrounded by grain boundary martensite. Figure 14 also depicts that the amount of martensite present in the microstructures is inadequate to control the grain coarsening in CGHAZ. Therefore, despite the partial solid-state phase transformation on cooling, the CGHAZ is characterized by a coarse grain size.

TEM micrographs of CGHAZ as shown in Fig. 15 reveal that the CGHAZ contains dispersed dislocation lines. The martensite laths are also present in CGHAZ, though the amount is less compared to the weld metal — Fig. 9. Again, the martensite laths that form in the CGHAZ are in a premature stage. A number of dislocation lines distributed from boundary to the interior of the ferrite grain in the CGHAZ are also observed. This indicates that distributed dislocations

Table 8 — Tensile Test Results of Notched Base Metal and Welded Joints

Sample Specification	YS (MPa)	Notch Tensile Strength (MPa)	NSR	Elongation	Location of Fracture
BM	458.8 ±5.77	660.3 ±12.63	1.37 ±0.03	10.8 ±1.26	BM
J1	584.8 ±7.32	865.2 ±6.73	1.853 ±0.03	23.5 ±0.82	BM
J2	588.3 ±8.43	871.3 ±10.67	1.838 ±0.01	22.4 ±0.87	BM
J3	587.5 ±11.23	869.7 ±9.88	1.845 ±0.01	22.9 ±1.03	BM
J4	593.4 ±9.11	874.3 ±11.27	1.831 ±0.02	22.2 ±0.91	BM

do not favor the formation of martensite laths. Rather, dislocation pileup acts as a precursor to the martensite formation. These dislocation lines are probably the result of local deformation caused by the residual stress (Ref. 21) during the weld thermal cycle. CGHAZ of J1 shows very little lath martensite formation along the grain boundary as illustrated in Fig. 15A. Interestingly, the lath martensite content increases with the increase in  $\text{CO}_2$  content — Fig. 15B–D. Therefore, the lath martensite present in different CGHAZ can be written in increasing

order as follows: J1→J2→J3→J4. The concentration of lath martensite present in CGHAZ can be explained by the interstitial diffusion mechanism of carbon into CGHAZ from weld metal because an increase in  $\text{CO}_2$  content increases the area of base metal fusion (Table 4) due to change in weld pool shape and thermal cycle that might act as a driving force to carbon diffusion in CGHAZ.

Meyer and duToit (Ref. 28) reported that the higher carbon content in the weld metal might increase the interstitial content of CGHAZ signifi-

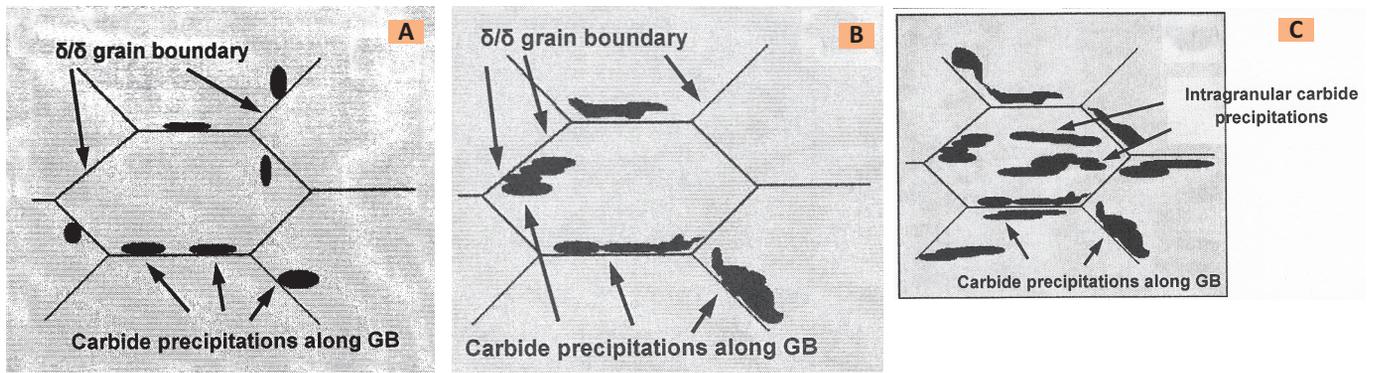


Fig. 12 — Schematic representations. A — Disrupted and small precipitations of carbide along the  $\delta/\delta$  grain boundary at 100% Ar shielding gas condition; B — precipitations of carbide along the  $\delta/\delta$  grain boundary increases with the addition of 5% to 10%  $\text{CO}_2$  in shielding gas mixture; C — grain boundary and intragranular carbide precipitation were observed with the addition of 20%  $\text{CO}_2$  in gas mixture.

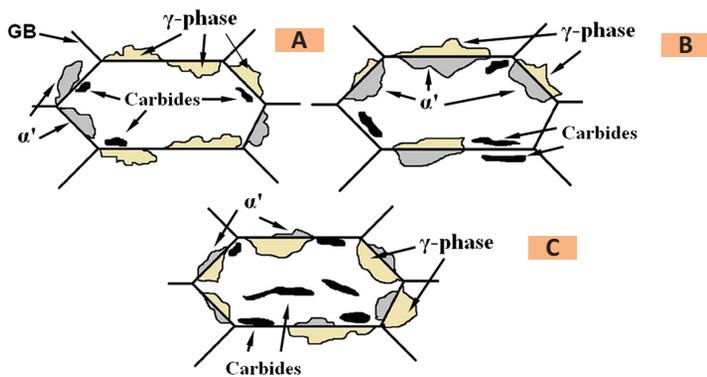


Fig. 13 — Schematic representation of three different types of microstructural combinations observed in the welds due to variation in  $\text{CO}_2$  content in shielding gas mixture with  $\text{Cr}_{eq}/\text{Ni}_{eq}$  ratios and MT temperatures. A — Stable austenite formation, low martensite content, and low carbide precipitation; B — metastable austenite formation, high martensite content, and moderate carbide precipitation; C — stable austenite formation, low martensite content, and high carbide precipitation.

cantly through fusion boundary diffusion during cooling from high temperature (1200° to 1300°C). In the present study, it was observed that the carbon content of the welds increased with the increase in  $\text{CO}_2$  content — Fig. 5. Therefore, it is likely that at the same heat input more carbon should diffuse through the fusion boundary into the CGHAZ region with the increase in  $\text{CO}_2$  content. Higher carbon content expands the  $\gamma$  loop to a certain extent and, hence, increases the  $\gamma$ -phase formation. The  $\gamma$ -phase formed at the high temperature is metastable in nature because of low nickel content in CGHAZ, and therefore further transformed (solid-state phase transformation, i.e.,  $\gamma \rightarrow \alpha'$ ) into lath martensite along the grain boundary during continuous cooling — Fig. 15.

The grain size of CGHAZ is also notably affected by different shielding gas compositions — Fig. 10. In general, CGHAZ produced coarse grains; although CGHAZ produced by pure Ar (J1) attributes maximum grain growth and became finer with an increase in  $\text{CO}_2$  content. Therefore, the grain size of different CGHAZ can be written in decreasing order as follows: J1→J2→J3→J4. The decreasing trend of grain coarsening with the increase in  $\text{CO}_2$  content can be explained by the formation of  $\gamma$ -phase and lath martensite along the ferrite grain boundaries. Higher  $\gamma$ -phase and lath martensite formation, associated with the diffused carbon content, can restrict the  $\delta$ -ferrite grain growth at the high peak temperatures experienced during welding (Ref. 29). The forma-

tion of lowest  $\gamma$ -phase and/or lath martensite along the grain boundary is unable to restrict the grain coarsening in the CGHAZ of J1, whereas, the increase in  $\text{CO}_2$  content increases the carbon diffusion and thus increases the  $\gamma$ -phase and lath martensite content, which ultimately increases the degree of grain fineness in CGHAZ.

### Correlation of Mechanical Properties with Microstructure

#### Microhardness

The microhardness values are plotted in Fig. 16 and the average microhardness of different welded zones are given in Table 6. The average hardness of weld metal (~350 HV) is higher than that of the HAZ (~316 HV) and BM (~195 HV). Furthermore, as expected, among the four types of welds, J2 and J3 having relatively higher martensite content (Fig. 6C) and finer grain size (Fig. 10), have provided slightly higher hardness. On the other hand, HAZ having coarser ferrite grains (Fig. 14) with lesser amount of lath martensite and separately placed dislocations provide lower hardness — Fig. 16. Interestingly, J1, having pure Ar shielding, had the lowest HAZ hardness, whereas hardness slightly increased with the increase in  $\text{CO}_2$  content. An increase in  $\text{CO}_2$  content increases the metastable  $\gamma$ -phase formation along the grain boundary at high temperature, which further transformed to lath martensite (through solid-state phase transformation) upon cooling

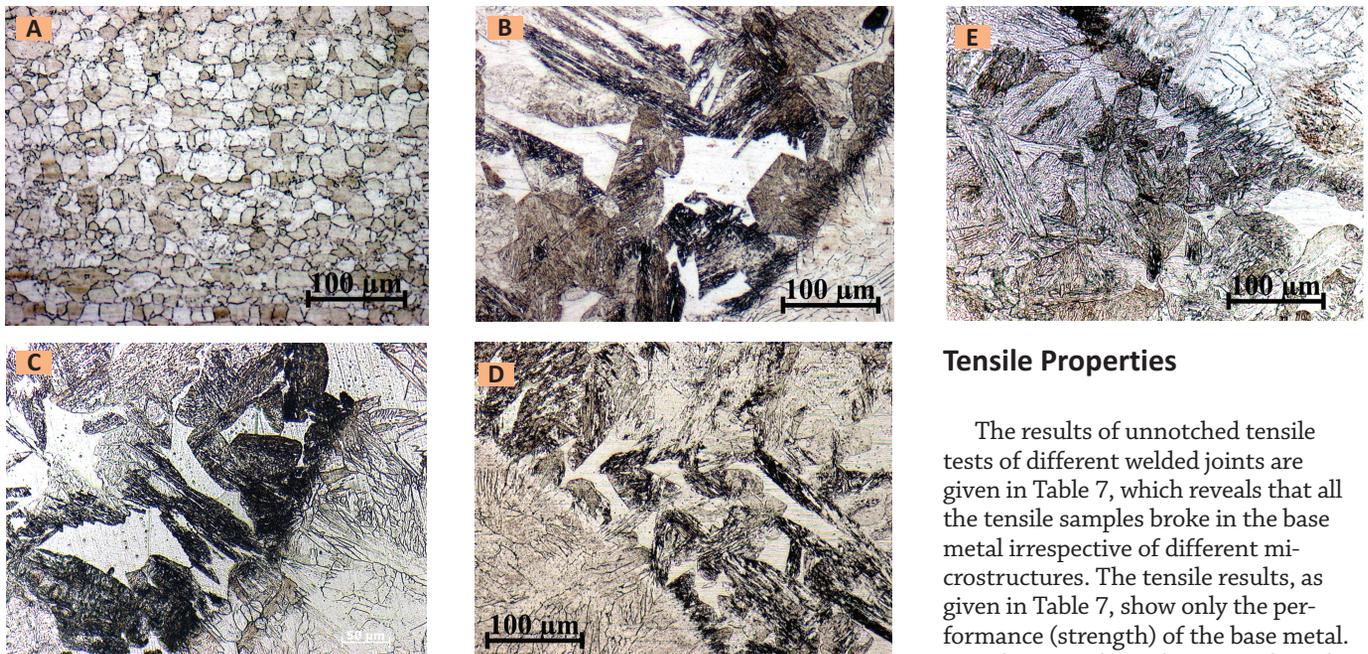


Fig. 14 — Optical micrograph. A — Base metal shows equiaxed ferrite grains and HTHAZ under different shielding gas compositions; B — J1; C — J2; D — J3; E — J4 shows massive or coarse ferrite grains enveloped with lath martensite.

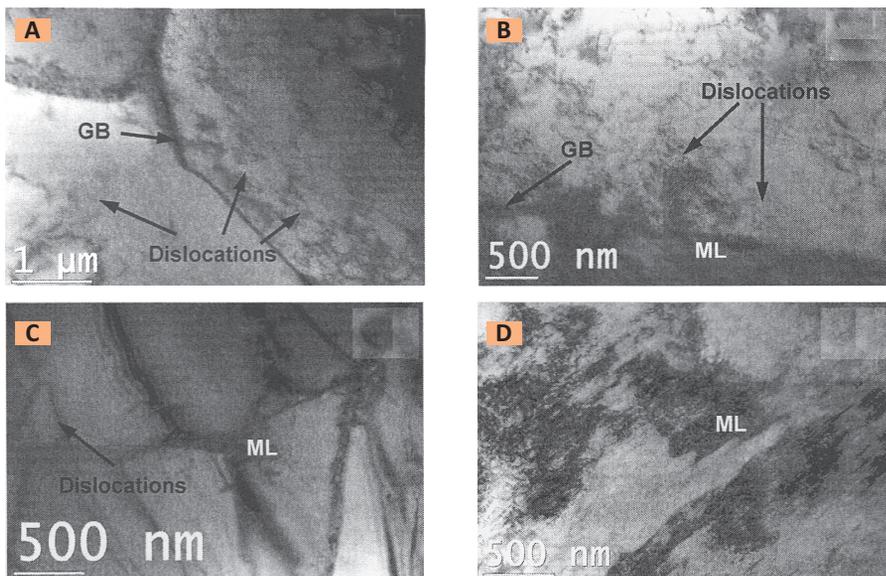
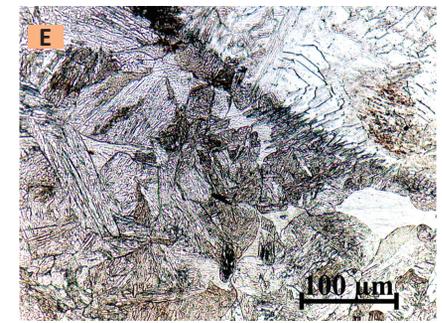


Fig. 15 — Bright field TEM micrograph of HTHAZ, A — J1; B — J2; C — J3; D — J4, shows the presence of dislocations along with lath martensite.

to room temperature. Phase transformation leads to the higher dislocation density in the respective HAZ regions (Fig. 15) resulting in comparatively finer grain structure (Fig. 10) and increases the hardness values. Again, more heterogeneity in hardness distribution is observed with weld J1. Hardness being a reflection of mi-

crostructure, heterogeneity in hardness distribution resulted from local microstructural variation. Since martensite transformation temperature of J1 is lower as derived from chemical composition, slight variation in local cooling rate may affect the formation of martensite laths leading to heterogeneity in hardness.



## Tensile Properties

The results of unnotched tensile tests of different welded joints are given in Table 7, which reveals that all the tensile samples broke in the base metal irrespective of different microstructures. The tensile results, as given in Table 7, show only the performance (strength) of the base metal. In order to find out the strength of the weld metal, notched tensile samples were tested and the test results are given in Table 8. The notch strength has been calculated as the maximum load divided by the cross-sectional area at the notch. The notch sensitivity of different welds has been expressed by the notch-strength ratio (NSR).

$$\text{NSR} = S_{\text{not}} \text{ (for notch specimen at maximum load)} / S_u \text{ (tensile strength for unnotched specimen)} \quad (9)$$

In spite of the notching effect, all the notched tensile samples broke in the base metal. Since all the welded samples broke in the base metal in notched tensile tests, tensile results therefore indicated that weld metal and even the HAZ are much stronger than the base metal. The strength of the weld metal is derived from its microstructure, which consists mostly of ferrite along with metastable  $\gamma$ -phase and lath martensite. The metastable  $\gamma$ -phase further transformed into martensite through stress/strain induced transformation, which ultimately increases the strength (Ref. 30). However, the percentage elongation of base metal is significantly higher (29.8%) than the welded unnotched samples (~23%) although both yield strength (YS) and ultimate tensile strength (UTS) are comparable (Table 7). This may be due to con-

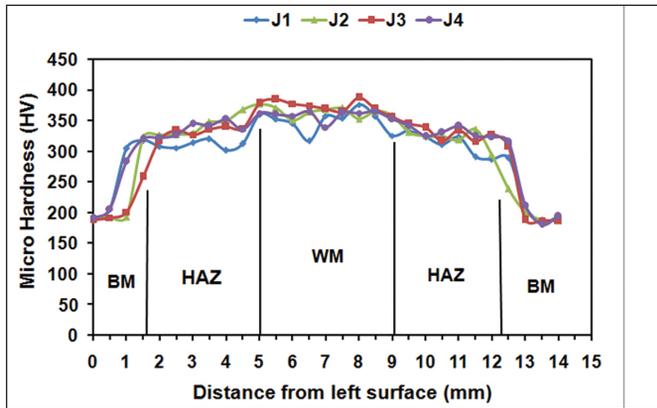


Fig. 16 — Vickers microhardness across the different weld joints.

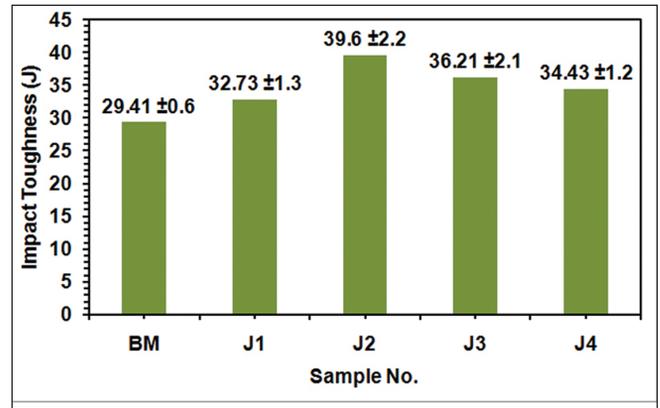


Fig. 17 — Impact toughness values of weld metals.

strain provided by the relatively harder weld metal and HAZ during deformation under tensile loading.

In the notched tensile test, however, YS, notch tensile strength, and percentage elongation of welded notched samples differ considerably although all the samples broke in the base metal (Table 8). The stress is concentrated in the weld metal due to notching effect and experienced strain hardening with the initial increase in tensile load, leading to increasing the strength. However, with further increasing the tensile load, the strain hardening effect becomes saturated and this facilitated the transmission of load to the adjacent base metal. As the base metal is incapable of bearing the load, failure takes place at the base metal.

### Toughness

Charpy impact toughness values of all the welded joints are illustrated in Fig. 17. The impact toughness of the base metal is 29.41 J and impact toughness values of welds J1, J2, J3, and J4 are 32.73, 39.6, 36.21, and 34.33 J, respectively. This clearly indicates there is an increase in weld metal toughness values compared to base metal irrespective of shielding gas conditions. However, among the four shielding gas conditions, the weld metal prepared with 5% CO<sub>2</sub> (J2) exhibited the highest impact toughness followed by J3, J4, and J1. Nevertheless, variations in toughness values among J1, J3, and J4 are trivial.

The weld metal toughness is undoubtedly dependent upon the several factors such as amount of metastable

austenite, martensite transformation, carbide precipitation, and grain size. In general, improved toughness of weld metal is due to the presence of higher martensite content together with equivalent grain structure compare to the base metal — Fig. 17.

Martensite colonies arrest secondary cleavages and increase total energy absorbed during fracture (Ref. 31). The grain growth of delta ferrite at high temperatures is also restricted by a higher fraction of austenite on the grain boundaries (which ultimately transform to martensite on cooling and under deformation). However, the impact toughness values of the weld metal show relatively complex behavior involving several dependent factors. In the present study, weld metal J1 with pure Ar shielding has a higher amount of stable austenite together with very less carbide precipitation along the grain boundary (Fig. 13A), resulting in relatively lower toughness. This phenomenon only indicates the dominant role played by the grain size and the lath martensite. Weld metal J1 has a comparatively coarse grain structure (Fig. 10) with a lower amount of lath martensite (Fig. 6), which ultimately resulted in a comparatively lower toughness by decreasing the absorbed energy during fracture. In welds J2 and J3, higher martensite formation (Fig. 6C) with fine grain structure (Fig. 10) eventually nullify other factors (i.e., metastable  $\gamma$ -phase and carbide precipitation) by hindering secondary cleavages during fracture and thus increases toughness. Interestingly, weld J4, even with higher carbide precipitation (Figs. 11

and 12), shows comparable toughness value with other welds. This is probably due to the fact that higher carbon content in weld J4 (Fig. 5) increases the amount of stable austenite by expanding the  $\gamma$  loop and enhances the toughness to some extent by taking priority over the precipitation. In addition, apart from microstructural constituents, inclusion content of the weld metal also manipulates the toughness values. In general, it is accepted that higher inclusion content in weld metal can drastically decrease the toughness values (Ref. 32). Again, inclusion content increases with the increase in oxygen potential (OP) of shielding gas mixtures. Accordingly, pure Ar shielding has zero OP and as the CO<sub>2</sub> content increases, OP increases simultaneously. Higher OP obviously increases the inclusion content in the weld metal, and it should decrease the toughness. However, based on the observed toughness, it can be assumed that the inclusion formed in the weld metal is very fine, which was reported to have almost negligible effect on the toughness of the weld metal (Ref. 33).

Additionally, SEM fractographs (Fig. 18) show the size and distribution of dimples on the surface of broken Charpy impact specimens. By comparing the fractographs in Fig. 18B and C, it is observed that the 5% and 10% CO<sub>2</sub> welds have mainly ductile rupture with very few cleavages, which clearly indicate the enhancement in toughness. Conversely, other welds have extensive distribution of cleavage facets with ductile rupture on the fracture surfaces, which undoubt-

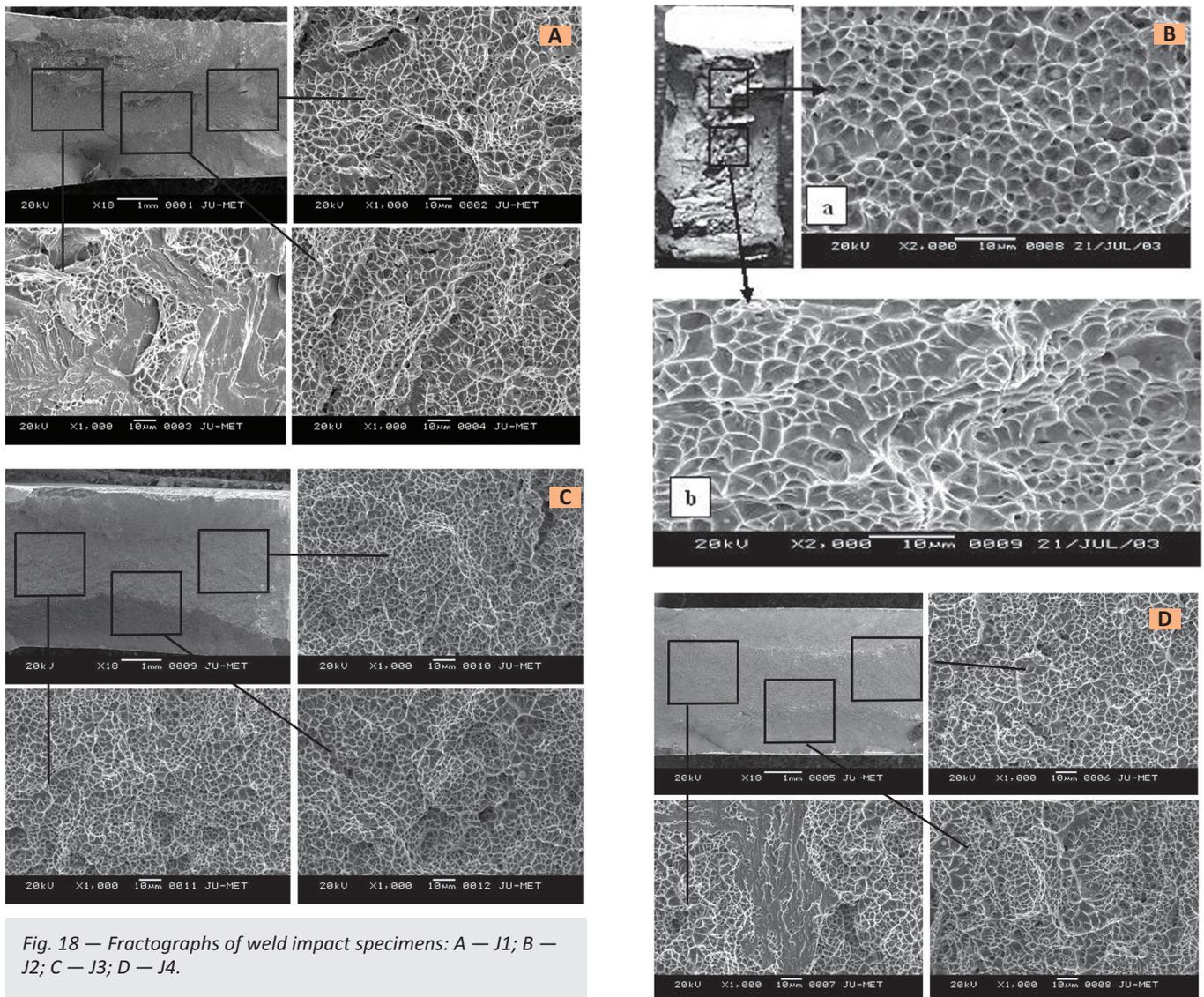


Fig. 18 — Fractographs of weld impact specimens: A — J1; B — J2; C — J3; D — J4.

edly support the close proximity of the toughness values as illustrated in Fig. 18A and D. The cleavage facets depict the reduction in toughness up to a certain extent but do not deteriorate so much because of the certain ductile nature of the rupture, which is incorporated by the microstructural constituents.

## Conclusions

From the present study, the following conclusions can be drawn:

1) Higher CO<sub>2</sub> content in shielding gas mixtures leads to an alteration in fluid flow mechanism, resulting in flatter, wider, and laterally deep penetrated bead profile, which ultimately increases dilution.

2) Welds J2 and J3 with 5% and

10% CO<sub>2</sub>, respectively, provide a higher amount of martensite along the grain boundary. The dominant path of martensite transformation is  $\gamma \rightarrow \alpha'$ . However,  $\gamma \rightarrow \epsilon \rightarrow \alpha'$  transformation is also realized in the case of pure Ar and 20% CO<sub>2</sub> mixtures. Also, the precipitation of M<sub>23</sub>C<sub>6</sub>-type carbides increases with higher CO<sub>2</sub> content.

3) Three types of microstructural combinations are possible in the weld metal. First, stable austenite is formed together with a lower amount of martensite formation and less carbide precipitation along the grain boundary. Second, metastable austenite together with a higher amount of martensite is formed and there is comparatively higher carbide precipitation. Third, stable austenite is formed together with low martensite and higher

precipitates. Again, the weld metal has a fine grain structure irrespective of shielding gas mixtures; however, the variation of grain size in the weld metal is probably controlled by the variation in  $\gamma$  phase and M<sub>23</sub>C<sub>6</sub> precipitation along the grain boundary.

4) In general, the high-temperature heat-affected zone of all the welded joints is characterized by coarse ferrite grains surrounded by the  $\gamma$ -phase and lath martensite. However, higher CO<sub>2</sub> content restricted grain coarsening in the CGHAZ up to a certain extent.

5) The weld metal is harder than the HAZ followed by the base metal. Differences among the weld metal hardness values are trivial with the change in shielding gas mixture. However, HAZ hardness slightly increases with the increase in CO<sub>2</sub> content.

6) All unnotched and notched tensile specimens failed in the base metal, indicating a higher strength for the weld metal and HAZ than the base metal.

7) The Charpy impact toughness of weld metal, in general, is better than the base metal. The welds J2 and J3 with 5% and 10% CO<sub>2</sub>, respectively, exhibited relatively higher impact toughness values than the other weld metal.

8) Finally, as a whole, it can be concluded that up to 10% CO<sub>2</sub> may be utilized in an Ar shielding gas mixture for fabricating welded joints of modified FSS (409M) using 308L filler metal in spray transfer mode without deteriorating microstructural or mechanical properties.

### Acknowledgments

The authors would like to gratefully thank the Council of Scientific and Industrial Research (CSIR), Pusa, New Delhi, India, for funding this research with a senior research fellowship. The authors would also like to thank Dr. G. Das of National Metallurgical Laboratory, Jamshedpur, and Mrs. D. Kanchanamala of IIT Madras, India, for their assistance in TEM work.

### References

- Mukherjee, M., and Pal, T. K. 2012. Influence of mode of metal transfer on microstructure and mechanical properties of gas metal arc-welded modified ferritic stainless steel. *Metallurgical and Materials Transactions A* 43: 1791–1808.
- Mukherjee, M., and Pal, T. K. 2012. Influence of heat input on martensite formation and impact property of ferritic-austenitic dissimilar weld metals. *Journal of Materials Science and Technology* 28: 343–352.
- Szumner, A., Jezierska, E., and Lublinska, K. 1999. Hydrogen surface effects in ferritic stainless steels. *Journal of Alloys and Compounds* 293–295: 356–360.
- Liao, M. T., and Chen, W. J. 1998. The effect of shielding gas compositions on the microstructure and mechanical properties of stainless steel weldments. *J. Mater. Chem. Phys.* 55: 145–151.
- Soderstrom, E. J., and Mendez, P. F. 2008. Metal transfer during GMAW with thin electrodes and Ar-CO<sub>2</sub> shielding gas mixtures. *Welding Journal* 87(5): 124-s to 133-s.
- Smith, A. A. 1971. *CO<sub>2</sub> Welding of Steel*, 3rd ed. Cambridge, UK: The Welding Institute.
- Mostafa, N. B., and Khajavi, M. N. 2006. Optimization of welding parameters for weld penetration in FCAW. *J. Achievement Mater. Manuf. Technol.* 16: 132–138.
- Karadeniz, E., Ozsarac, U., and Yildiz, C. 2007. The effect of process parameters on penetration in gas metal arc welding processes. *Materials and Design* 28: 649–656.
- Jonsson, J., Murphy, P. G., and Szekely, A. B. 1995. Influence of oxygen additions on argon shielded gas metal arc welding processes. *Welding Journal* 74(2): 48-s to 58-s.
- Subramaniam, D. R., and White, S. 2001. Effect of shield gas composition on surface tension of steel droplets in a gas-metal-arc welding arc. *Metallurgical and Materials Transactions B* 32: 313–318.
- Kotecki, D. J. 2000. A martensite boundary on the WRC-1992 Diagram – Part 2: The effect of manganese. *Welding Journal* 79(12): 346-s to 354-s.
- Dai, Q. X., Cheng, X. N., Zhao, Y. T., Luo, X. M., and Yuan, Z. Z. 2004. Design of martensite transformation temperature by calculation for austenitic steels. *Materials Characterization* 52: 349–354.
- Talonen, J., Aspegren, P., and Hanninen, H. 2004. Comparison of different methods for measuring strain induced  $\alpha'$ -martensite content in austenitic steels. *Materials Science and Technology* 20: 1506–1512.
- Zacharia, T., Eraslan, A. H., Aidun, D. K., and David, S. A. 1989. Three-dimensional transient model for arc welding process. *Metallurgical Transactions B* 20B: 645–659.
- Zacharia, T., Eraslan, A. H., and Aidun, D. K. 1988. Modeling of non-autogenous welding. *Welding Journal* 67(1): 18-s to 27-s.
- Stenbacka, N. 1990. The influence of shielding gas on cored wires. *Welding Journal* 69(11): 43–45.
- Pires, I., Quintino, L., and Miranda, R. M. 2007. Analysis of the influence of shielding gas mixtures on the gas metal arc welding metal transfer modes and fume formation rate. *Materials and Design* 28: 1623–1631.
- Kotecki, D. J. 1997. Ferrite determination in stainless steel welds: Advances since 1974. *Welding Journal* 76(1): 24-s to 37-s.
- Mangonon, P. L., and Thomas, G. 1970. The martensite phases in 304 stainless steel. *Metallurgical Transactions* 1: 1577–1586.
- Murr, L. E., and Standhammer, K. P. 1982.  $\alpha'$ -Martensite morphology in shock-loaded type 304 stainless steel. *Scripta Metallurgica* 16: 713–716.
- Brooks, J. W., Loretto, M. H., and Smallman, R. E. 1979. In situ observations of the formation of martensite in stainless steel. *Acta Metallurgica* 27: 1829–1838.
- Elmer, J. W., Allen, S. M., and Eagar, T. W. 1989. Microstructural development during solidification of stainless steel alloys. *Metallurgical Transactions A* 20A: 2117–2131.
- Pryds, N. H., and Huang, X. 2000. The effect of cooling rate on the microstructure formed during solidification of ferritic steels. *Metallurgical and Materials Transactions A* 31A: 3155–3166.
- Castro, R., and Tricot, R. 1964. Study of the isothermal transformations in 17% Cr stainless steels, 2: Influence of carbon and nitrogen. *Metal Treatment and Drop Forging* 31: 469.
- Lippold, J. C., and Kotecki, D. J. 2005. *Welding Metallurgy and Weldability of Stainless Steels*. Wiley-Interscience publication, 1st ed., 109–110.
- Mukherjee, M., and Pal, T. K. 2013. Effect of modes of metal transfer and microstructure on corrosion behavior of welded modified ferritic stainless steel in acidic environments. *Journal of Applied Electrochemistry* 43: 347–365.
- Di Schino, A., Barteri, M., and Kenny, J. M. 2003. Grain size dependence of mechanical, corrosion and tribological properties of high nitrogen stainless steels. *Journal of Materials Science* 38: 3257–3262.
- Meyer, A. M., and du Toit, M. 2001. Interstitial diffusion of carbon and nitrogen into heat-affected zones of 11–12% chromium steel welds. *Welding Journal* 80(12): 275-s to 280-s.
- Zaayman, J. J. 1992. The heat-affected zone toughness of welds in 11 to 12 percent chromium steels. *M Engg UP* 31–71: 76–93.
- Lakshminarayanan, A. K., Shanmugam, K., and Balasubramanian, V. 2009. Effect of welding processes on tensile and impact properties, hardness and microstructure of AISI 409M ferritic stainless joints fabricated by duplex stainless steel filler metal. *Journal of Iron and Steel Research International* 16: 66–72.
- Gooch, T. G., and Ginn, B. J. 1988. Report from the cooperative research program for research members only. The Welding Institute, Cambridge, England, 6: 3–30.
- Vaidya, V. 2002. Shielding gas mixtures for semiautomatic welds. *Welding Journal* 81(9): 43–48.
- Marshall, A. W., and Farrar, J. C. M. 2001. Welding of ferritic and martensitic 11–14% Cr steels. *Welding in the World* 45: 32–55.